

Article

Phase Composition Effects on Dynamic Behavior and Strain Rate Sensitivity in Metastable β -Ti Alloys

Tao Wang ^{1,2}, Yong Feng ^{1,2}, Xianghong Liu ^{1,2}, Kaixuan Wang ², Shaoqiang Li ² and Feng Zhao ^{3,*} 

¹ State Key Laboratory of Solidification Processing, Northwestern Polytechnical University, Xi'an 710072, China; wang-tao@c-wst.com (T.W.); yfeng@c-wst.com (Y.F.); xhliu@c-wst.com (X.L.)

² Western Superconducting Technologies Co., Ltd., Shaanxi Province Engineering Laboratory for Aerial Material, Xi'an 710018, China; kingsin@c-wst.com (K.W.); sqli_wst@163.com (S.L.)

³ Institute for Advanced Study, Chengdu University, Chengdu 610106, China

* Correspondence: zhaofeng@cdu.edu.cn

Abstract: In this study, high strain rate tension tests are conducted to determine and compare the dynamic mechanical behaviors and deformation mechanisms of different phase composition α - β metastable β -Ti alloys using a split Hopkinson tension bar. Two typical bimodal equiaxed $\alpha_p + \beta$ and lamellar $\alpha_s + \beta$ Ti-45551 alloy microstructures are formed through different hot working and thermal processing for investigating the effect of phase composition or microstructure on mechanical properties and strain rate sensitivity. It is demonstrated that dislocation nucleation and motion in the α/β phase and dislocation tangle or pile up at the α/β interface are typical deformation modes in both of the typical dual-phase Ti alloys at quasi-static loading conditions. Under dynamic loading, both the strength and ductility show a clearly positive strain rate dependence, which is directly related to dislocation activation in the $\alpha + \beta$ Ti-45551 alloy. Based on microstructure characterizations, it is shown that deformation twinning starts to become a major deformation mechanism in equiaxed $\alpha_p + \beta$ microstructures under dynamic loading conditions. However, deformation twins are not favored in the lamellar $\alpha_s + \beta$ Ti-45551 alloy due to its nano phase size. Finally, the mechanical behaviors and strain rate sensitivity are strongly dependent on the phase composition of metastable β -Ti alloys.

Keywords: metastable β -Ti alloys; strain rate sensitivity; mechanical behavior; phase composition



Citation: Wang, T.; Feng, Y.; Liu, X.; Wang, K.; Li, S.; Zhao, F. Phase Composition Effects on Dynamic Behavior and Strain Rate Sensitivity in Metastable β -Ti Alloys. *Materials* **2022**, *15*, 4068. <https://doi.org/10.3390/ma15124068>

Academic Editor: Jan Haubrich

Received: 7 May 2022

Accepted: 1 June 2022

Published: 8 June 2022

Publisher's Note: MDPI stays neutral with regard to jurisdictional claims in published maps and institutional affiliations.



Copyright: © 2022 by the authors. Licensee MDPI, Basel, Switzerland. This article is an open access article distributed under the terms and conditions of the Creative Commons Attribution (CC BY) license (<https://creativecommons.org/licenses/by/4.0/>).

1. Introduction

Because of the high strength to weight ratio, the broad range of service temperatures, and the excellent corrosion resistance, metastable β -Ti alloys have widespread application in the aviation, aerospace, and automotive industries [1–3]. Generally, the microstructure of metastable β -Ti alloys consists of α and β phases. Generally, the high strength always is attributed to the Hexagonal close-packed (HCP) α phase, and the ductility comes from the Body-centered cubic (BCC) β phase. Thus, the superior strength–ductility synergy and microstructure tailoring method are governed by the α and β phase composition of metastable β -Ti alloys [4].

By means of thermo-mechanical processing routes, many kinds of microstructures can be produced, including equiaxed $\alpha_p + \beta$, lamellar $\alpha_s + \beta$, and equiaxed $\alpha_p +$ lamellar $\alpha_s + \beta$ bimodal microstructures. As a result, the phase composition or microstructure heterogeneity exhibits a great effect on the mechanical behaviors of these metastable β -Ti alloys. Many efforts have been proposed to describe the relationship between mechanical properties, microstructural evolution, and deformation mechanisms in the metastable β -Ti alloys. Generally, a high density of dislocation tends to pile up against the α/β interfaces during plastic deformation under quasi-static loading conditions [5]. Recently, based on studies of the α phase size effect on deformation modes of the Ti-5553 alloy, it has been shown that dislocation spacing and dislocation type are controlled by the

size and distribution of the α phase [6,7]. Moreover, with the decreasing of lamellar α_s thickness, the strength of lamellar $\alpha_s + \beta$ -Ti alloys increases following a Hall–Petch relationship [8,9]. The phase size, volume fraction, morphology, and distribution of the α phase are essential microstructure parameters which govern the deformation modes and/or mechanical behaviors [10]. As a result, for improving the strength and ductility, it is necessary to understand the phase composition effects on mechanical behaviors during plastic deformation.

For structural engineering applications, where high strength metastable β -Ti alloys are always subjected to high strain rate loading conditions, the role and effect of phase composition on mechanical properties must be understood. However, the focus of prior studies on mechanical behaviors of metastable β -Ti alloys was primarily under quasi-static loading conditions. Generally, these alloys have shown a strong strain rate sensitivity (SRS) at ambient temperature and low strain rates [11–13]. Few studies have been conducted on the dynamic deformation behaviors of metastable β -Ti alloys. Therefore, a systematic study of the phase composition on the dynamic mechanical behaviors and plastic deformation of metastable β -Ti alloys is required.

The present work aimed to investigate the difference in the mechanical behaviors of a metastable β -Ti alloy under dynamic loading at a range of strain rates (1×10^{-3} – $4 \times 10^3 \text{ s}^{-1}$). Moreover, the effects of phase composition on the mechanical behaviors and plastic deformation under dynamic tensile loading were investigated. In this work, a series of quasi-static and dynamic tensile tests was conducted on a metastable β -Ti alloy at room temperature. The mechanical behaviors and deformation mechanisms were carefully investigated.

2. Experimental Procedure

2.1. Materials

In this work, the as-received material was Ti-45551 (mass: Al, 4.00%; Mo, 4.99%; V, 5.03%; Cr, 5.01%; Nb, 1.03%; Ti, balance). The Ti-45551 alloy ingot was first fabricated by cold crucible induction levitation melting. The β -transus temperature was about 800 °C. The β -field forging and the multi-axial $\alpha + \beta$ field forging were conducted by hydraulic press. The Ti-45551 alloy was solution treated (ST) above β -transus temperature (870 °C) for 2 h followed by air cooling (AC), and then aging at 525 °C for 4 h and AC. Scanning electron microscope and electron back scattered diffraction (EBSD) were used to examine the microstructure of the Ti-45551 alloy. Figure 1a shows the typical $\alpha + \beta$ bimodal phase microstructure. Figure 1b illustrates the inverse pole figure and phase-mapping of the ST and aged Ti-45551 alloy. The resulting microstructure included about 24% equiaxed primary α_p phase (grain size $\sim 2 \mu\text{m}$) and equiaxed β phase grain ($\sim 40 \mu\text{m}$). In order to get an additional insight into the microstructure, Figure 2a,b shows that the applied heated treatment resulted in the microstructure of a primary α_p and α_s lamellar microstructure.

In order to obtain a uniform lamellar α_s phase, equiaxed $\alpha_p + \beta$ samples were then aged at 360 °C for 8 h and AC, followed by another aging at 550 °C for 8 h. The microstructure of the two-stage aged Ti-45551 is shown in the Scanning electron microscope (SEM) and bright field Transmission electron microscope (TEM) image in Figure 2c,d. Figure 2c shows the α_s lamellar structure evenly lies on the equiaxed β grains. The number density of the lamellar α_s phase was very high. The width of the lamellar α_s phase was about 30–60 nm, while its length was about 200 nm to 2 μm , as seen in Figure 2d. Moreover, in both the equiaxed $\alpha_p + \alpha_s + \beta$ and lamellar $\alpha_s + \beta$ bimodal microstructures, tangled dislocations were found near the interface of α/β .

2.2. Mechanical Properties

The quasi-static tensile tests were performed using an Mechanical tests system (MTS) testing system (Sansi, Chengdu, China) with a strain rate of 10^{-3} s^{-1} at room temperature. During the tensile tests, the elongation was recorded by an extensometer with gauge length

of 12 mm. As tensile samples break in the working area of the extensometer, the total strain histories are recorded by the testing systems under quasi-static loading.

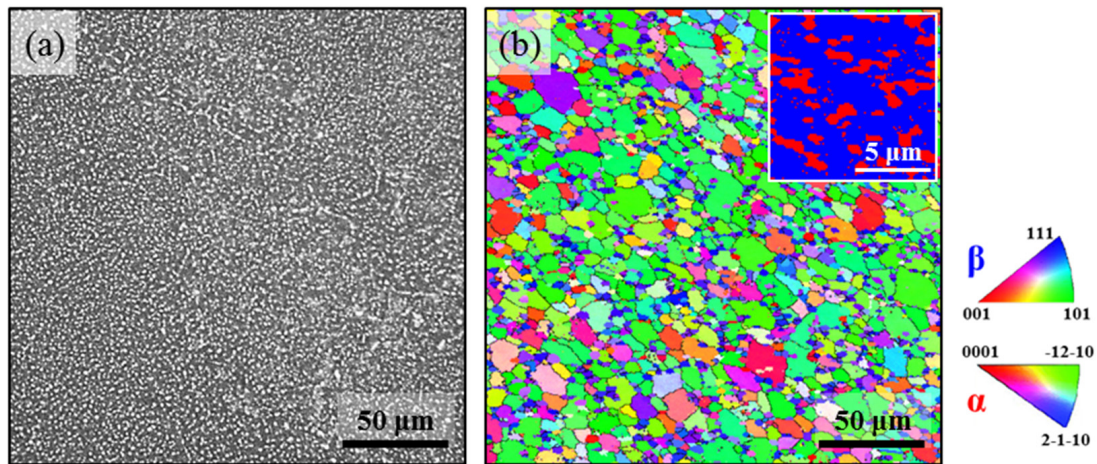


Figure 1. The microstructure of solution-treated Ti-45551 alloy: (a) SEM micrograph; (b) EBSD IPF map and phase map.

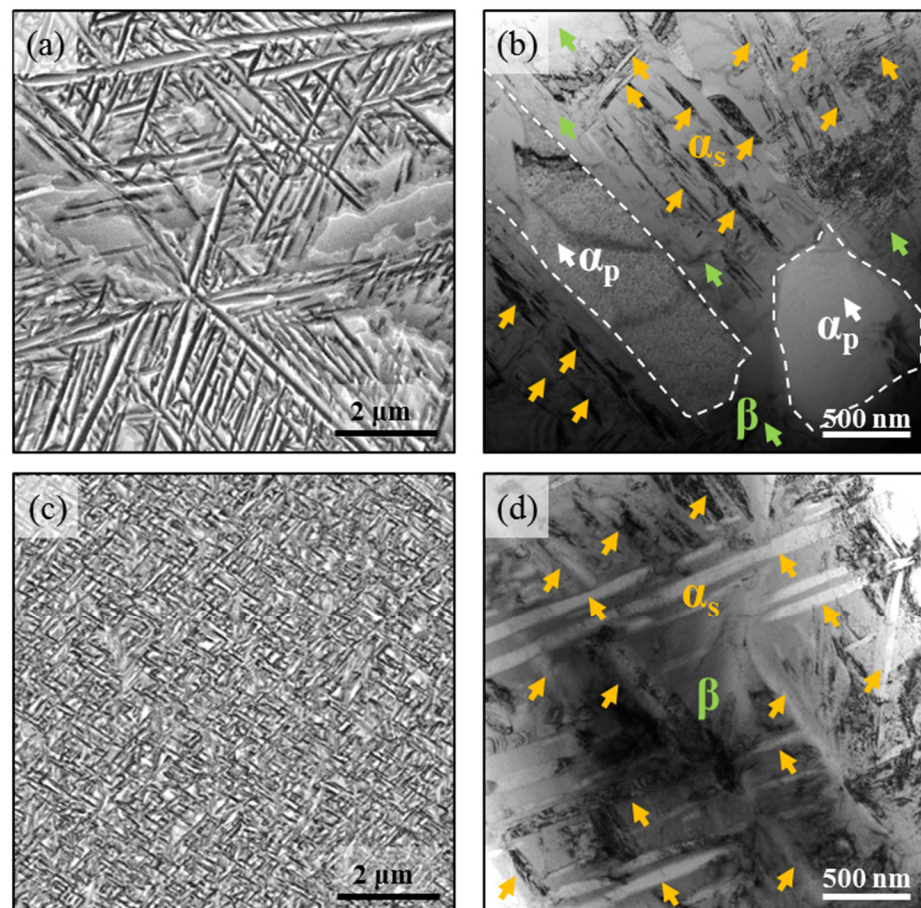


Figure 2. Typical microstructures of Ti-45551 alloy after different heat treatment. (a,b) Ti-45551 alloy after being aged at 360 °C for 8 h; (c,d) Ti-45551 alloy after being aged at 360 °C for 8 h + aged at 550 °C for 8 h. The yellow arrows represent α_s , green arrows represent β and white arrows represent α_p .

The dynamic tensile tests were performed at strain rates of ($\sim 6 \times 10^2 \text{ s}^{-1}$, $2 \times 10^3 \text{ s}^{-1}$, and $4 \times 10^3 \text{ s}^{-1}$) by using a standard Split Hopkinson tension bar (SHTB) system at RT. In order to ensure the repeatability of the tensile test data, at least three tests were conducted at a certain strain rate. Figure 3a shows the schematic illustration of SHTB, which was used in this work. During dynamic loading, an elastic stress wave is generated when the projectile strikes the incident bar. As the stress wave reaches the interface of the incident bar/specimen, it partially propagates through the sample into the transmission bar as a transmitted wave. In the meantime, the incident wave partially reflects back into the incident bar as a reflection wave at the incident bar/specimen interface. The reflected wave and transmitted wave were recorded using strain gages, which were fixed on elastic bars, as seen in Figure 3. During the test, the incident, reflection, and transmission voltage–time signals were recorded by the data acquisition system. According to the one-dimensional stress wave theory, the true stress, true strain, and strain rate of each impact can be calculated as follows:

$$\sigma_S(t) = E \left(\frac{A}{A_S} \right) \varepsilon_T(t) \quad (1)$$

$$\varepsilon_S(t) = \frac{2C_0}{l_s} \int_0^t \varepsilon_R(t) dt \quad (2)$$

$$\dot{\varepsilon}_S(t) = \frac{2C_0}{l_s} \varepsilon_R(t) \quad (3)$$

where ε_R is the reflection strain, ε_T is the transmission strain, E is Young's modulus, A is the cross-sectional area, C_0 is the longitudinal wave speed of the bars, A_s is the cross-sectional area of the specimen, and l_s is the length of the specimen. The details of the SHTB technique can be found elsewhere [14,15].

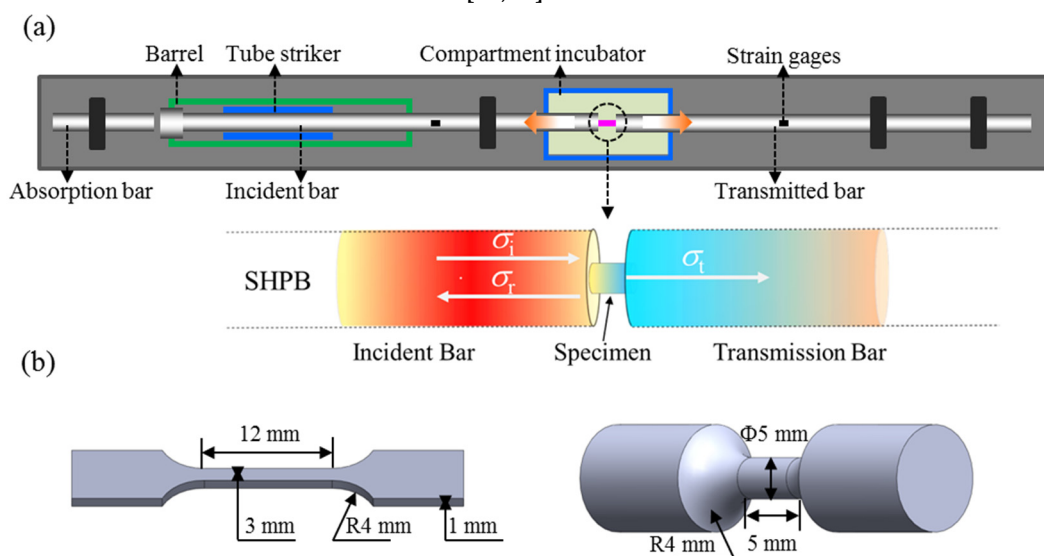


Figure 3. Schematic of split Hopkinson tensile bar (SHPB) and stress wave history during dynamic tension (a) and (b) the precise dimensions of the Ti alloy samples for quasi-static and dynamic tensile tests.

The precise dimensions of the Ti alloy samples for quasi-static and dynamic tensile tests are shown in Figure 3b respectively.

2.3. Microstructure Characterization

In this work, the microstructure characterizations were conducted by SEM (JEOL, Tokyo, Japan), Electron backscatter diffraction EBSD (JEOL), and TEM (JEOL) at different strain rates at room temperature. For the EBSD characterization, the samples were first mechanically grinded with 400–1200 grit SiC paper and then mechanically polished by

using 0.2 μm diamond paste. Subsequently, each sample was electrolytically polished to remove surface strain. The EBSD data were obtained by HKL Channel 5 analysis software (Version 5.12, 2019, Oxford instruments, Oxford, UK). The EBSD images were acquired under the following conditions: a 20 kV acceleration voltage and a 0.1 μm scan step size on a rectangular scan grid. After plastic deformation, the TEM samples were taken from the deformed region. The bright field and the high-resolution images of the deformed Ti alloy were acquired by JEOL F200 (JEOL). TEM disk samples were used after mechanical polishing and thinned to perforation using precision ion thinning treatment.

3. Result and Discussion

3.1. Phase Composition Effects on Mechanical Behaviours

Generally, tensile properties are affected by the microstructure, such as the phase volume fraction, phase size, morphology of equiaxed α_p and lamellar α_s , and transformed β phase. Based on the two typical phase compositions or microstructures ($\alpha_{p,s} + \beta$, $\alpha_s + \beta$) of Ti-45551 alloy, the effect of microstructure on mechanical behaviors and deformation mechanisms was systematically investigated.

Figure 4a presents the true stress–true strain curves of the $\alpha_{p,s} + \beta$ Ti-45551 alloy at different strain rates at room temperature. Obviously, the dynamic true stress–true strain curves of the Ti-45551 alloy exhibited some oscillations due to the stress wave reflection between the surfaces of specimens and incident bar. Figure 4a presents the yield strength of the $\alpha_{p,s} + \beta$ Ti-45551 alloy, which increased by 240 MPa as the strain rate increased from $1 \times 10^{-3} \text{ s}^{-1}$ to $4 \times 10^3 \text{ s}^{-1}$ at room temperature. Furthermore, there was no obvious change in elongation and strain hardening capability.

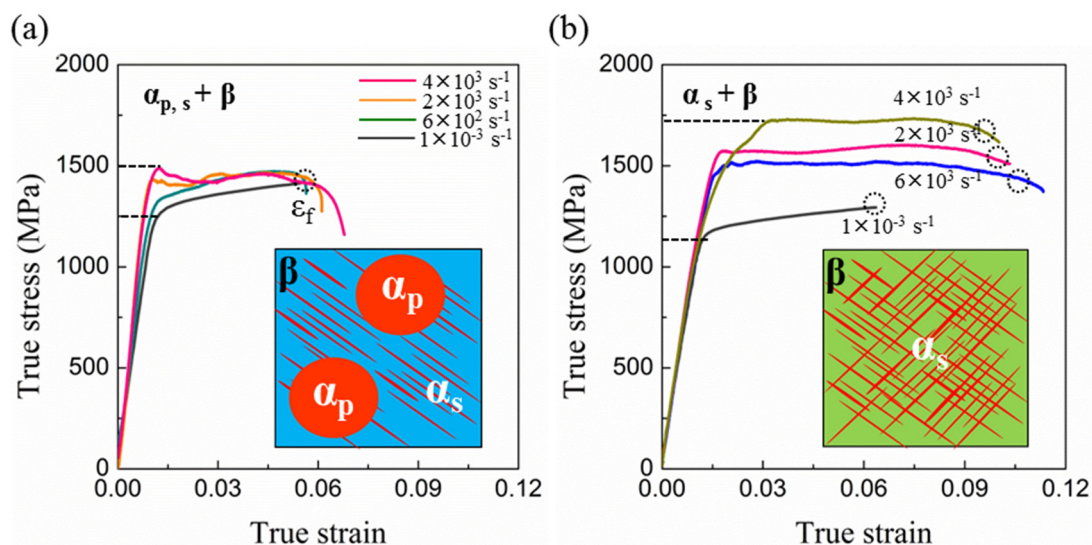


Figure 4. Mechanical behaviors of two kinds of α - β metastable β -Ti alloys at different strain rates. (a) Tensile stress–true strain curves of $\alpha_{p,s} + \beta$ Ti-45551 and (b) tensile true stress–true strain curves of $\alpha_s + \beta$ Ti-45551. The quasi-static curves (strain rate, 10^{-3} s^{-1}) were obtained from MTS testing system and dynamic curves were obtained from SHPB (strain rate $\sim 6 \times 10^2 \text{ s}^{-1}$, $2 \times 10^3 \text{ s}^{-1}$, and $4 \times 10^3 \text{ s}^{-1}$).

The true stress–true strain curves of the lamellar $\alpha_s + \beta$ phase Ti-45551 alloy at a range of strain rates is shown in Figure 4b. As shown in Figure 4b, the yield stress of the lamellar $\alpha_s + \beta$ phase Ti-45551 alloy was about 1120 MPa at $1 \times 10^{-3} \text{ s}^{-1}$, lower than the yield strength of the $\alpha_{p,s} + \beta$ Ti-45551 alloy (1260 MPa). This difference in yield strength may come from a Hall–Petch relationship with the size of the lamellar α_s of the Ti-45551 alloy. Under quasi-static loading conditions, Figure 4b shows that the lamellar $\alpha_s + \beta$ phase Ti-45551 alloy exhibits a clear strain hardening capability. Moreover, the yield strength (σ_y) and failure strain (ε_f) were about 1120 MPa and 6.1% at room temperature. As shown in

Figure 4b, the Ti-45551 alloy exhibited a higher yield strength and larger ductility, implying that the mechanical properties of the lamellar $\alpha_s + \beta$ phase Ti-45551 alloy exhibit a strong strain rate dependence. Furthermore, it should be noticed that the lamellar $\alpha_s + \beta$ phase Ti-45551 alloy shows a clear strain softening capability at high strain rate loading conditions. Similar rate dependences have been reported in Ti6Al4V and AM50 alloys [16]

The slope factor of the yield strength versus the logarithm of the strain rate is the strain rate sensitivity (SRS) of materials [17]. Moreover, SRS coefficients for plastic deformation under different strain rate loadings could be described as follows:

$$m = \frac{d \ln \sigma}{d \ln \dot{\epsilon}} \quad (4)$$

Figure 5 shows the variation of SRS for the Ti-45551 alloy with different phase compositions or microstructures. The lamellar $\alpha_s + \beta$ phase Ti-45551 alloy shows a lower SRS coefficient than the $\alpha_{p,s} + \beta$ Ti-45551 alloy.

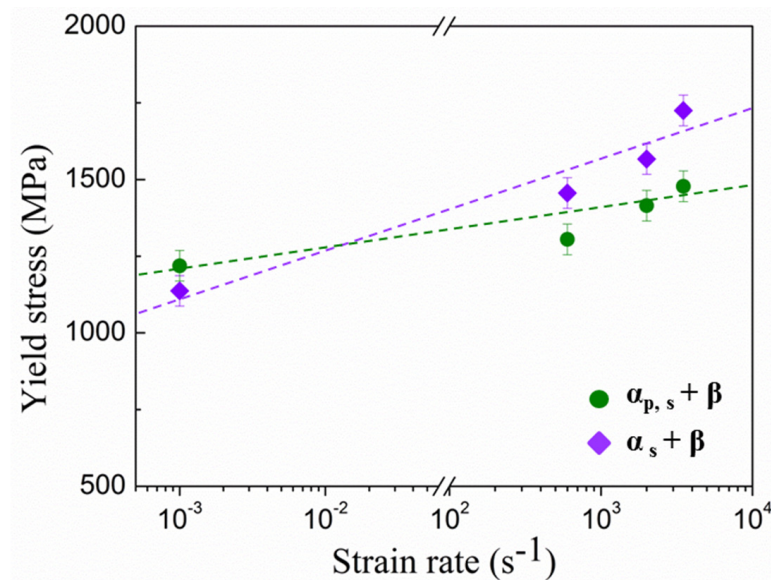


Figure 5. Yield strength of two kinds of α - β metastable β -Ti alloys at different strain rates. The quasi-static data (strain rate, 10^{-3} s^{-1}) were obtained from MTS testing system and dynamic data were obtained from SHPB (strain rate $\sim 6 \times 10^2 \text{ s}^{-1}$, $2 \times 10^3 \text{ s}^{-1}$, and $4 \times 10^3 \text{ s}^{-1}$).

3.2. Phase Composition Effects on Deformation Modes

Figure 6 shows the basic deformation modes, including dislocation slips and deformation twinning, in the HCP α phase and BCC β phase during plastic deformation at room temperature [18]. When the HCP α phase deforms at room temperature, traditionally only two independent slip systems can be activated in the basal plane. However, the BCC β phase exhibits a total of forty-eight slip systems at room temperature, i.e., twelve (112) [111] type slip systems, twelve (110) [111] type slip systems, and twelve (123) [111] type slip systems [19]. For polycrystalline materials, at least five independent slip systems are needed for the homogenous plastic deformation of materials [20]. As a consequence, the ductility of dual-phase Ti alloys is majorly governed by the HCP α phase, which exhibits limited slip systems. However, under shock loading, deformation twinning can act as a complementary deformation mode in accommodating the local plastic deformation in HCP material. Deformation twinning with the type of $\langle 10\text{-}12 \rangle \{10\text{-}11\}$ compression twin and $\langle 10\text{-}11 \rangle \{10\text{-}12\}$ extension twin always accommodates the local plastic strain along the c-axis.

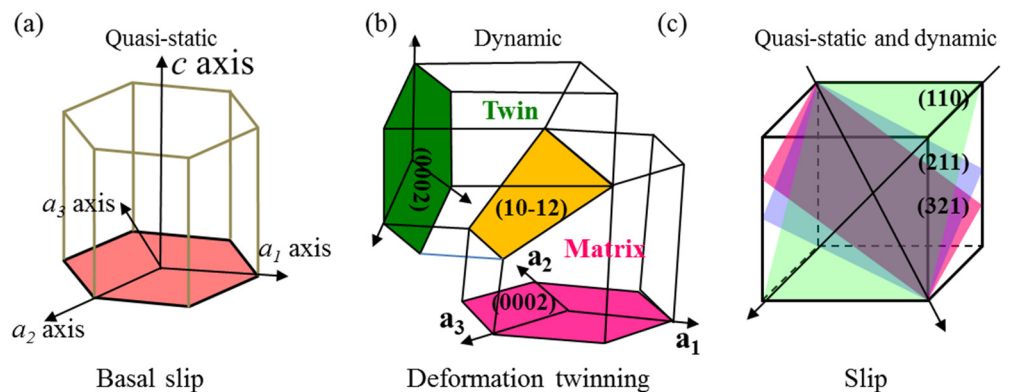


Figure 6. Schematic diagram of deformation modes in α - β Ti alloys. (a) HCP α phase at quasi-static loading; (b) HCP α phase at dynamic loading; (c) BCC β phase at quasi-static and dynamic loading.

Focusing on the deformation mechanisms of Ti-45551 under different loading conditions, we characterized the deformation mechanisms of the Ti-45551 samples after tensile tests. Figure 7 shows the major deformation mode of the Ti-45551 alloy with different phase compositions at quasi-static loading. From the bright field TEM image, the major deformation mechanisms are dislocation slip in both the $\alpha_{p,s} + \beta$ and lamellar $\alpha_s + \beta$ phase Ti-45551 alloys because high density dislocation can be found in deformed areas. Figure 7a shows that a high dislocation density structure can be found in the α_s lamellae and α_s/β interface. However, the dislocation density in the equiaxed α_p phase is very low due to their limited slip systems at room temperature. A clear dislocation pile up can be found in the equiaxed α_p phase, as shown in Figure 7b. The dislocations that nucleate and accumulate at the phase boundaries would be impeded and have their movement stopped by the α phase, which contributes to the high strength and strain hardening effect of Ti-45551 alloys. Moreover, the nonuniform distribution of dislocation density can easily introduce stress concentration in the α/β interface, and then result in the low ductility of Ti-45551. Figure 7c also shows a lot of dislocation tangles (high density dislocation structure), such as those distributed in the α/β interface and β grains. Moreover, the dislocation density is also very low in the lamellar α_s phase, as shown in Figure 7d.

Figure 8 shows the major deformation mode in both the $\alpha_{p,s} + \beta$ and lamellar $\alpha_s + \beta$ phase Ti-45551 alloys under dynamic loading. After tension tests, there was a lot of deformation twinning in the equiaxed α_p phase, as shown in Figure 8a,b. Most deformation twins appeared as plates with a thickness of about 100 nm and across the entire equiaxed α_p phase, which is expected due to the dynamic loading. During plastic deformation, the twin boundaries within the primary α particle produce more nucleation sites for dislocation and impede dislocation motion. Thus, the dislocation density in the primary α particle is high, as seen in Figure 8b. The higher strength of the $\alpha_{p,s} + \beta$ Ti-45551 alloy is attributed to the additional hindering effect of the twin boundaries on dislocation motion under dynamic loading.

For the lamellar $\alpha_s + \beta$ phase Ti-45551 alloy, the plasticity of the lamellar microstructure is still primarily controlled by dislocation slip. Compare with the equiaxed α_p phase, the width of the lamellar α_s was only about 30–60 nm, which largely limits the twin nucleation and propagation even under shock loading. However, it can be observed that the dislocation density was similar in the lamellar α_s and β phase during the dynamic deformation process, as seen in Figure 8a. High dense dislocations are stacked in the lamellar α_s . During dynamic deformation, more dislocations are activated from α_s/β boundaries and slip in the HCP lamellar α_s . The lamellar α_s phase can also contribute more plastic deformation under shock loading. Therefore, lamellar $\alpha_s + \beta$ phase Ti-45551 can exhibit a large ductility under dynamic loading conditions.

3.3. Phase Composition Effects on Failure Modes

It is widely accepted that fractographic features are helpful to analyze the fracture behavior and related performance of the materials. Therefore, for understanding the effect of strain rate on the tensile fracture mechanism, the tensile fracture morphology of the $\alpha_s + \beta$ and lamellar $\alpha_s + \beta$ phase Ti-45551 alloy under quasi-static and dynamic loading conditions were carefully observed.

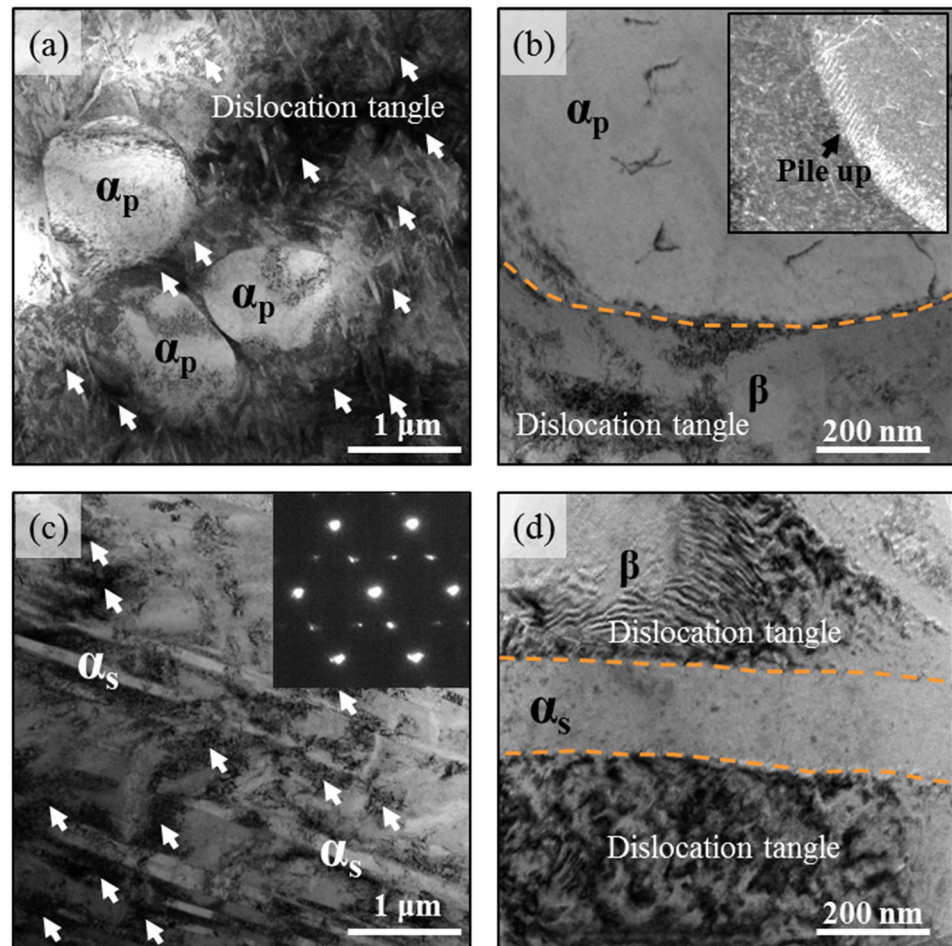


Figure 7. Deformation micromechanisms in two kinds of α - β metastable β -Ti alloys at quasi-static loading. (a) Bright field TEM image of deformed $\alpha_{p,s} + \beta$ Ti-45551 and its details (b); (c) bright field TEM image of deformed $\alpha_s + \beta$ Ti-45551 and its details (d). The white arrows represent dislocation tangles.

Figure 9a shows the fractography of the tensile $\alpha_s + \beta$ Ti-45551 specimen under quasi-static loading (the arrow represents the shear direction). Figure 9a shows a mix fracture mode of dimple and crack under quasi-static loading. The cracks are parallel or perpendicular to the shear direction in the fracture areas. The typical fracture surface of the tensile $\alpha_s + \beta$ Ti-45551 specimen under dynamic loading ($4 \times 10^3 \text{ s}^{-1}$) is shown in Figure 9b. The major failure mode was dimples. The depth of the dimples was much deeper than that under the quasi-static loading and without obvious cracking, as shown in Figure 9b. Therefore, the shear failure mechanism is the major fracture mode of the Ti-45551 specimens under both quasi-static and dynamic loading conditions. Compared with the failure modes of the $\alpha_s + \beta$ Ti-45551 specimen, the $\alpha_{p,s} + \beta$ Ti-45551 alloy showed less cracking under quasi-static loading and more uniform dimples under dynamic loading. Moreover, the fractography of the Ti alloy also proves that the $\alpha_{p,s} + \beta$ Ti-45551 alloy exhibits an excellent ductility, especially under shock loading.

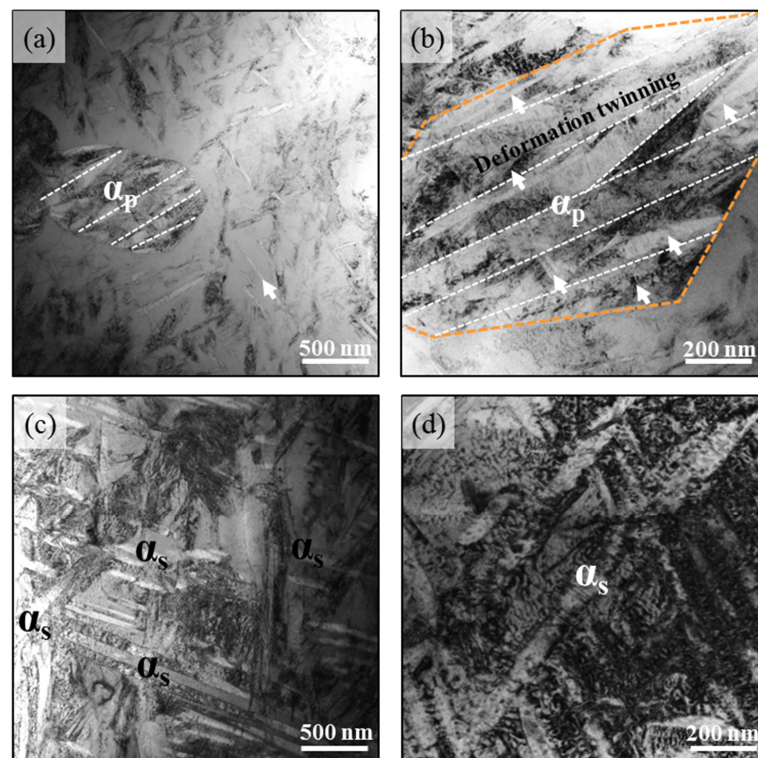


Figure 8. Deformation micromechanisms in two kinds of α - β metastable β -Ti alloys at dynamic loading. (a) Bright field TEM image of deformed $\alpha_{p,s} + \beta$ Ti-45551 and its details (b); (c) bright field TEM image of deformed $\alpha_s + \beta$ Ti-45551 and its details (d). The white arrows represent deformation twinning.

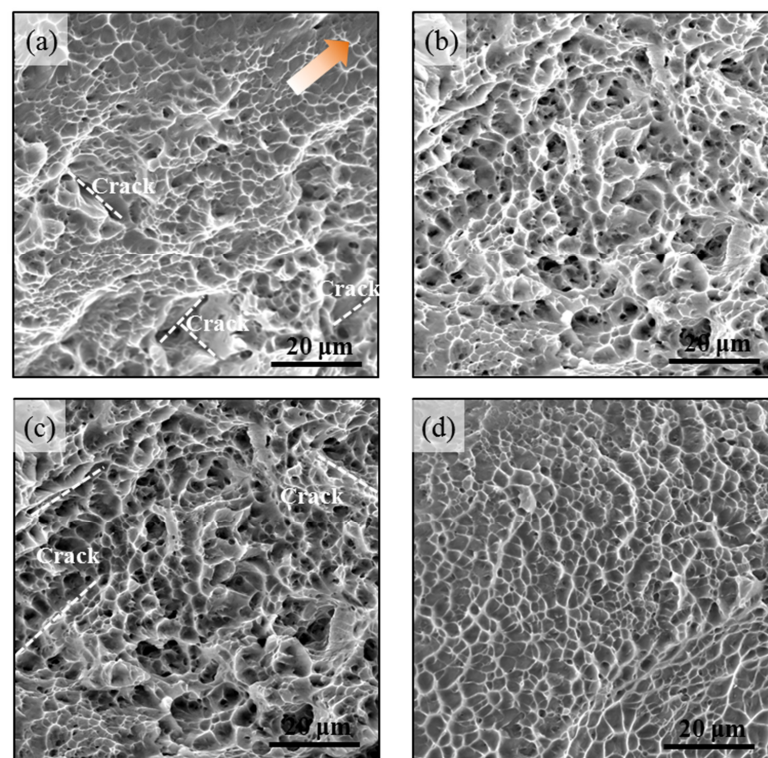


Figure 9. Fractography of $\alpha_s + \beta$ and $\alpha_{p,s} + \beta$ Ti alloy at quasi-static and dynamic loading conditions. The $\alpha_s + \beta$ Ti alloy under (a) quasi-static loading and (b) dynamic loading. The $\alpha_{p,s} + \beta$ Ti alloy under (c) quasi-static loading and (d) dynamic loading. The arrow represents the shear direction.

4. Conclusions

The mechanical behaviors, deformation mechanisms, and failure behaviors of dual-phase Ti-45551 alloy with different phase compositions under quasi-static and dynamic loading conditions at room temperature were reported. The results from the tensile testing show that the lamellar $\alpha_s + \beta$ phase Ti-45551 alloy exhibits higher strain rate sensitivity. Under dynamic loading, the strength and ductility increase under a high strain rate. Microstructure observations reveal that the transition from dislocation slip to deformation twinning occurs in the equiaxed α_p phase of the $\alpha_{p,s} + \beta$ Ti-45551 alloy during dynamic plasticity. Moreover, the lamellar α_s phase can also contribute more plastic deformation through more dislocation activated in the α_s phase under shock loading. The analysis of the fracture morphology showed that ductile dimples along the shear direction is the major fracture mode under both quasi-static and dynamic loading. Ti-45551 samples show more and deeper dimples, which represent more uniform plastic deformation at a high strain rate.

Author Contributions: Conceptualization, F.Z. and Y.F. data curation, T.W.; formal analysis, T.W. and Y.F.; investigation, T.W., K.W. and X.L.; methodology, X.L. and S.L.; writing—original draft, F.Z. and T.W.; writing—review and editing, F.Z. and Y.F. All authors have read and agreed to the published version of the manuscript.

Funding: Applied Basic Research Programs of the Science and Technology Department of Sichuan province (No. 2020YJ0479).

Institutional Review Board Statement: Not applicable.

Informed Consent Statement: Not applicable.

Data Availability Statement: Data sharing is not applicable to this article.

Acknowledgments: We acknowledge support from the Applied Basic Research Programs of the Science and Technology Department of Sichuan province.

Conflicts of Interest: The authors declare no conflict of interest.

References

1. Wang, Y.L.; Hao, M.Y.; Li, D.; Liang, Q.L.; Wang, D.; Zheng, Y.F.; Sun, Q.Y.; Wang, Y.Z. Enhanced mechanical properties of Ti-5Al-5Mo-5V-3Cr-1Zr by bimodal lamellar precipitate microstructures via two-step aging. *Mater. Sci. Eng. A* **2022**, *829*, 142117. [[CrossRef](#)]
2. Boyer, R.R. An overview on the use of titanium in the aerospace industry. *Mater. Sci. Eng. A* **1996**, *213*, 103–114. [[CrossRef](#)]
3. Jiang, B.Z.; Emura, E.; Tsuchiya, K. Microstructural evolution and its effect on the mechanical behavior of Ti-5Al-5Mo-5V-3Cr alloy during aging. *Mater. Sci. Eng. A* **2018**, *731*, 239–248. [[CrossRef](#)]
4. Qin, D.Y.; Zhao, F.; Li, Y.L. The conflicts between strength and ductility of bimodal Ti-5553 alloy with fine equiaxial prior β grains. *Mater. Sci. Eng. A* **2022**, *841*, 143074. [[CrossRef](#)]
5. Suri, S.; Viswanathan, G.B.; Neeraj, T.; Hou, D.H.; Mills, M.J. Room temperature deformation and mechanisms of slip transmission in oriented single-colony crystals of an α/β titanium alloy. *Acta Mater.* **1999**, *47*, 1019–1034. [[CrossRef](#)]
6. Zheng, Y.; Sosa, J.S.; Williams, R.E.A.; Wang, Y.; Banerjee, R.; Fraser, H.L. The role of omega phase in non-classical homogeneous precipitation of the alpha phase in beta-titanium alloys. *Scripta Mater.* **2016**, *111*, 81–84. [[CrossRef](#)]
7. Nag, S.; Zheng, Y.; Williams, R.E.A.; Devaraj, A.; Boyne, A.; Wang, Y.; Collins, P.C.; Viswanathan, G.B.; Tiley, J.S.; Muddle, B.C.; et al. Non-Classical homogeneous precipitation mediated by compositional fluctuations in titanium alloys. *Acta Mater.* **2012**, *60*, 6247–6256. [[CrossRef](#)]
8. Semiati, S.L.; Bieler, T.R. The effect of alpha platelet thickness on plastic flow during hot working of Ti-6Al-4V with a transformed microstructure. *Acta Mater.* **2001**, *49*, 3565–3573. [[CrossRef](#)]
9. Maruyama, K.; Yamada, N.; Sato, H. Effects of lamellar spacing on mechanical properties of fully lamellar Ti—39.4mol%Al alloy. *Mater. Sci. Eng. A* **2001**, *319–321*, 360–363. [[CrossRef](#)]
10. Clément, N.; Lenain, A.; Jacques, P.J. Mechanical property optimization via microstructural control of new metastable beta titanium alloys. *JOM* **2007**, *59*, 50–53. [[CrossRef](#)]
11. Waheed, S.; Zheng, Z.B.; Balint, D.S.; Dune, F.P. Microstructural effects on strain rate and dwell sensitivity in dual-phase titanium alloys. *Acta Mater.* **2019**, *162*, 136–148. [[CrossRef](#)]
12. Zheng, Z.; Waheed, S.; Balint, D.S.; Dune, F.P. Slip transfer across phase boundaries in dual phase titanium alloys and the effect on strain rate sensitivity. *Int. J. Plast.* **2018**, *104*, 23–38. [[CrossRef](#)]

13. Ran, C.; Chen, P.W.; Li, L.; Zhang, W.F.; Liu, Y.L.; Zhang, X. High-strain-rate plastic deformation and fracture behaviour of Ti-5Al-5Mo-5V-1Cr-1Fe titanium alloy at room temperature. *Mech. Mater.* **2018**, *116*, 3–10. [[CrossRef](#)]
14. Mishra, A.; Martin, M.; Thadhani, N.N.; Kad, B.K.; Kenik, E.A.; Meyers, M.A. High-strain-rate response of ultra-fine-grained copper. *Acta Mater.* **2008**, *56*, 2770–2783. [[CrossRef](#)]
15. Meyers, M.A. *Dynamic Behavior of Materials*; Wiley-Interscience: New York, NY, USA, 1994; pp. 323–326.
16. Rittel, D.; Wang, Z.G. Thermo-mechanical aspects of adiabatic shear failure of AM50 and Ti6Al4V alloys. *Mech. Mater.* **2008**, *40*, 629–635. [[CrossRef](#)]
17. Bintu, A.; Vincze, G.T.; Picu, R.C.; Lopes, A.B.; Bdkin, I. Scale dependence of the strain rate sensitivity of Twinning-Induced Plasticity steel. *Mater. Sci. Eng. A* **2016**, *674*, 98–103. [[CrossRef](#)]
18. Zheng, Z.; Balint, D.S.; Dunne, F.P.E. Discrete dislocation and crystal plasticity analyses of load shedding in polycrystalline titanium alloys. *Int. J. Plast.* **2016**, *87*, 15–31. [[CrossRef](#)]
19. Kumar, N.N.; Tewari, R.; Durgaprasad, P.V.; Dutta, B.K.; Dey, G.K. Active slip systems in bcc iron during nanoindentation: A molecular dynamics study. *Comput. Mater. Sci.* **2013**, *77*, 260–263. [[CrossRef](#)]
20. Karewar, S.; Gupta, N.; Groh, S.; Martinez, E.; Caro, A.; Srinivasan, S.G. Effect of Li on the deformation mechanisms of nanocrystalline hexagonal close packed magnesium. *Comput. Mater. Sci.* **2017**, *126*, 252–264. [[CrossRef](#)]